

www.acsaem.org Article

Effects of Graphene Interface on Potassiation in a Graphene-Selenium Heterostructure Cathode for Potassium-Ion Batteries

Vidushi Sharma* and Dibakar Datta





ACCESS

Metrics & More

Article Recommendations

Supporting Information

Difficult Intercalation

Wrapped

Layered

Se-Graphene Interface

Se x in K, Se

ABSTRACT: Selenium (Se) cathodes are an exciting emerging high energy density storage system for potassium-ion batteries (KIB), where potassiation reactions are less understood. Here, we present an atomic-level investigation of a K_x Se cathode enclosed in hexagonal lattices of carbon (C) characteristic of a layered graphene matrix and multiwalled carbon nanotubes (MW-CNTs). Microstructural changes directed by the graphene–substrate in the K_x Se cathode are contrasted with those in the graphene-free cathode. Graphene's binding affinity for long-chain polyselenides (Se₃ = -2.82 eV and Se₂ = -2.646 eV) at low K concentrations and ability to induce enhanced reactivity between Se and K at high K concentrations are investigated. Furthermore, intercalation voltage for graphene-enclosed K_x Se cathode reaction intermediates is calculated with K_2 Se as the final discharged product. Our results indicate a single-step reaction near a voltage of 1.55 V between K and Se cathode. Findings in the paper suggest that operating at higher voltages (\sim 2 V) could result in the formation of reaction intermediates where intercalation/deintercalation of K could be a challenge, and therefore cause irreversible capacity losses in the battery. The primary issue here is the modulating favorability of graphene surface toward discharging of Se cathode due to its differential preferences for K–Se reaction intermediates. A comparison with a graphene-free cathode highlights the substantial changes a van der Waals (vdW) graphene interface can bring in the atomic structure and electrochemistry of the K_x Se cathode.

KEYWORDS: Selenium Cathode, Heterostructure Electrodes, Potassium-Ion Battery, Graphene, Density Functional Theory, Interface

1. INTRODUCTION

Current innovations in the energy sector are focused on balancing the world energy consumption with clean energy solutions. Massive research and development efforts have been made in the past few decades to advance lithium-ion battery (LIB) stature to the primary energy storage for most engineering applications, including electronic devices, transportation, wearables, etc. ^{1,2} The rarity of Li and cost associated with development of LIBs strongly advise the use of low-cost complements such as sodium-ion batteries (NIBs) and potassium-ion batteries (KIBs) in applications where maximizing energy and power is not essential such as in small-scale energy applications. ³ In particular, KIBs have garnered interest as low cost complements of LIBs owing to the relative earthly abundant battery precursor materials. ^{4–7} The energy storage

mechanism in KIB is similar to "rocking chair" operation in LIBs, except for the respectively larger ion carriers that greatly differentiate the electrode intercalation mechanism and diffusion kinetics in KIB battery systems. This suggests careful tailoring of the structural design of electrodes³ for next-generation sustainable KIB batteries.

Among low-cost alternatives to Li for energy storage, K has a lower standard reduction potential, which is closer to Li

Received: April 19, 2023 Accepted: August 3, 2023



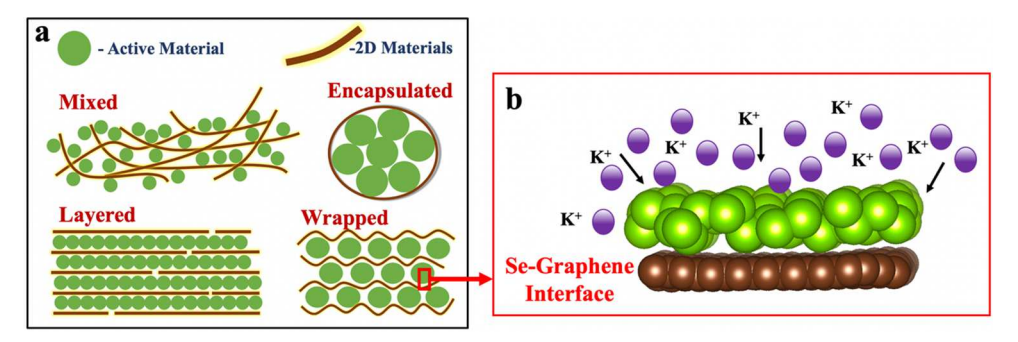


Figure 1. (a) Schematic representations of various heterostructure electrode designs with active materials and two-dimensional (2D) substrate such as graphene. (b) Atomic representation of the interface formed between active material Se and graphene in electrodes.

 $(-3.04 \text{ V } E^0 = \text{Li}^+/\text{Li}^- < -2.93 \text{ V } E^0 = \text{K}^+/\text{K}^- < -2.71 \text{ V } E^0 =$ Na⁺/Na⁻).³ This permits KIBs to operate at higher potentials with better energy density than NIBs.8 Moreover, the ionic mobility of K remains unhindered by its weight and is competitive to Li.9 On the electrode front, the commercial graphite anode used in LIB can be customized easily for KIB. K intercalated graphite is found to be stable even at a high alkali density of KC₈. The electrochemical analysis by Komaba et al. demonstrated graphite anode to have 244 mA h g⁻¹ reversible capacity for KIB in the 0-0.3 V range. Likewise, most commercially acceptable LIB anodes perform well for KIBs at relatively safer voltages.⁸ However, KIB cathodes become rather challenging to design due to the large size of the K ion. Transition metal layered oxide cathodes exhibit fast capacity fading in KIB because it is not easy to extract or reintercalate large K ions without any structural damage. 11 Layered birnessite K_{0.3}MnO₂ was one of the first layered oxide cathodes investigated for KIB by Vaalma et al. 12 in nonaqueous electrolyte, which only showed a reversible capacity of 65 mA h g⁻¹ between 3.5 and 1.5 V and 57% capacity retention. Instead, metal-organic frameworks (MOFs) are preferred alternatives to layered oxides as KIB cathodes. Pore sizes on the MOF are adjustable and promising for reversible K storage. Eftekhari et al. introduced K containing MOF called Prussian Blue (PB) cathode KFe₄^{III}[Fe^{II} (CN)₆], which could achieve 78.62 mA h g⁻¹ reversible capacity and only 12% capacity fade post 500 cycles.⁶ This stability marked PB as a prospective cathode for KIB and encouraged experimental electrochemical studies on several PB analogs. 13-16 Despite all efforts, high energy density cathodes still remain a major limiting factor in the development and adoption of KIB.

Chalcogenides like sulfur (S) and selenium (Se) store metal ions by conversion reactions that benefit energy densities. 17-22 However, these promising electrodes suffer from poor reversibility due to dissolution of reaction intermediates in the electrolyte and pulverization caused by large volume expansions. $^{17-22}$ Se is comparatively heavier, less reactive, and more electroconductive than S, 23,24 which imply that Se-based cathodes can have good electron transport and better control over shuttle effects if well engineered with a confining composite matrix. Liu et al. were the first to report performance of the Se cathode confined in carbonized polyacrylonitrile for KIB in 2017.²⁵ Active Se in the composite maintained a reversible capacity of 396 mA h g⁻¹ with K₂Se as a final discharged product. One added problem identified for K-Se batteries is the limited reactivity of both metals due to their large atomic size.²⁶ The strategy of confining Se in carbon (C) allotropes to control surface reactivity, phase transition,

and volume change in Se cathode has been well explored for LIBs and next-generation metal batteries. 20,21,27-36 However, the role of Se supporting C matrix goes beyond polyselenide confinement to providing an interface for easy expansion and contraction of Se during battery cycles. 37,38 Interestingly, refined hexagonal C lattice such as graphene (Gr) have the advantage of a slippery van der Waals surface that is shown to be effective in combating stresses in alloying electrodes upon ion storage, thereby improving the cycle life of the composite electrode. We previously reported the detailed characterization of the Se-Gr interface and its promising potential in mitigating interfacial stresses due to low interface adhesion (0.43 J/m^2) , 38 which was comparable to the silicon—(Si–) Gr system reported by Basu et al.³⁷ As such, using a graphenebased supporting matrix for Se cathode can achieve major electrode design targets like high electronic conductivity, physical confinement, large surface area, and alleviated volumetric and mechanical stresses.³⁸ However, the involvement of graphene in the electrochemistry of the K-Se battery is still less understood in the literature.

In the present work, we further explore the effects of interface presented by graphene to the Se cathode in a heterostructure electrode for application in next-generation KIB battery using computational methods. Latest simulation results have confirmed that the hexagonal lattice of C has a strong chemical affinity for K₂Se.²⁷ Therefore, we use K₂Se as the final discharged product of Se and compare the electrochemical voltage profile of the graphene-free Se cathode with the graphene-supported Se cathode. K intercalation and distribution are modeled in reaction intermediates between Se cathode and discharged product K₂Se for graphene-free as well as graphene-supported configurations. Microstructural changes at the graphene-K_xSe interface are investigated and further decomposed into Se-K clusters, whose binding energy with the graphene-substrate is calculated. Next, we throw some light on influence of graphene interface on electrochemical mechanism in Se-K cathode. We calculate the operational voltage to direct a single-step K2Se cathode discharging in a graphene enclosure. Substantial electrochemical changes that a graphene interface brings in the cathode without any covalent bonding with Se-K have been highlighted.

2. METHODOLOGY

2.1. Structure of Graphene-Supported Se Cathode. Two-dimensional (2D) materials such as graphene can form

Two-dimensional (2D) materials such as graphene can form heterostructure electrodes with active materials by multiple design strategies shown in Figure 1a including mixed, wrapped, encapsulated, and layered approaches. Though the exact

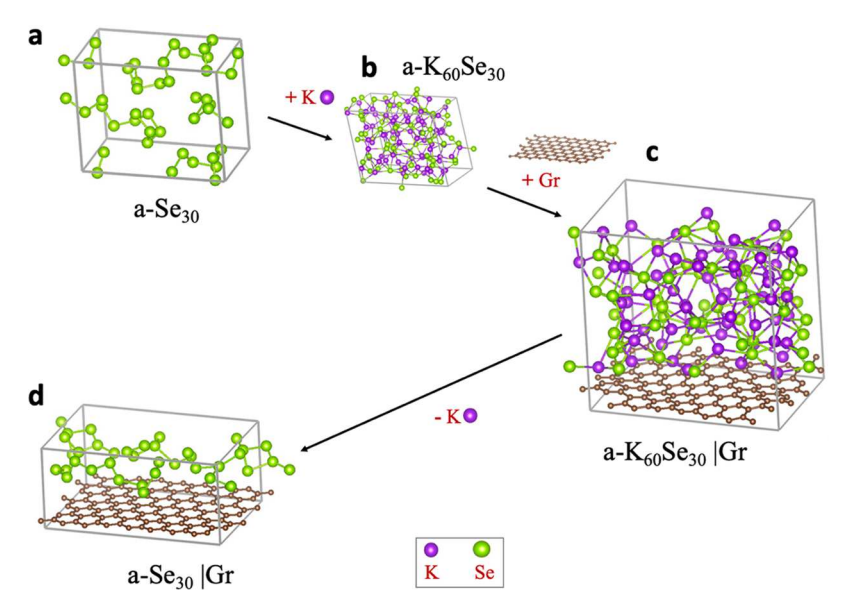


Figure 2. (a) Atomic representation of initial optimized amorphous Se $(a-Se_{30})$ generated from crystalline Se with computational quenching. The structure is dominated by disintegrated forms of Se rings as chains with nearest neighboring distance of ~2.4 Å. (b) Miniaturized view of $a-K_{60}Se_{30}$ $(a-K_2Se)$ generated after complete potassiation (discharging). The volume is expanded by 183.52%. (c) Atomic representation of $a-K_{60}Se_{30}/Gr$ $(a-K_2Se/Gr)$ system. Graphene with surface area equivalent to the base of $a-K_{60}Se_{30}$ was added in the z dimension. (d) Completely charged $a-Se_{30}/Gr$ cathode after potassium removal. The structure once again forms Se chains that are slightly condensed toward graphene surface.

chemical steps for experimentally preparing these electrode designs can deviate, the general approach involves infusing Se in graphene-based matrix at high temperature conditions followed by condensation. Sha et al. reported synthesis of a layer-by-layer stacked Se—graphene cathode by a high energy ball milling procedure. During the process, graphene gets fragmented, while crystalline Se turns amorphous and distributes across the graphene surface. These variations in macroscopic designs of the Se-Gr heterostructures majorly influence K diffusion pathways, mechanical stability, and electrolyte—electrode interface stability. However, if we zoom into atomic scale of these systems (Figure 1b), the electrochemical properties of the interface formed between Se cathode and graphene will stay consistent across the design space. Our study presents an atomic-level investigation of Se—Gr composites/heterostructures as cathodes.

Amorphous Se (a-Se) was derived by computational quenching of monoclinic selenium-containing Se₈ rings that break to form differently sized polymeric chains with a Se–Se bond length of 2.4 Å. The complete computational modeling and characterization of a-Se and a-Se/Gr have been reported in our previous study.³⁸ In battery systems, Se is mostly present in amorphous form with Se_n chains (n = 2 to 8).³⁶ Alternatively, if originally used in crystalline form, Se₈ rings are converted to Se_n chains after the first battery cycle and remain so for the rest of the battery life.⁴² Structural parameters such as interatomic bond lengths, bond angles, and dihedral angles are comparable among pristine Se allotropes,^{43,44} yet graphene matrix surface can direct the aligned distribution of Se.

To generate 3D periodic configurations of a- K_x Se cathode supported over graphene–substrate, we started with an optimized amorphous a-Se₃₀ system (Figure 2a) and sequentially added 6 K atoms at a time until a- K_{60} Se₃₀ (a- K_{2} Se) is achieved (Figure 2b). After each potassium addition step, K atoms were allowed to diffuse in the cathode during an ab initio molecular dynamics simulation (AIMD) run and then

relaxed with density functional theory (DFT) until energyoptimized a-K_xSe structures were obtained. Volume of the simulation cell was allowed to be adjusted in all dimensions. Between initial Se and final a-K₆₀Se₃₀ (Figure 2a,b), 183.52% volume expansion was noted. The simulation cell's base also expanded during potassiation, and the updated x-ydimensions were used to determine the graphene substrate's size. The final a-K₆₀Se₃₀ bulk configuration was placed on top of a periodic graphene lattice containing 96 sp² hybridized carbon atoms with an interfacial gap of ~2.8 Å to form a- $K_{60}Se_{30}/Gr$ interface (a- K_2Se/Gr). Note that the surface area of graphene-substrate was equivalent to the x-y surface of final a-K₆₀Se₃₀. We further let the atoms diffuse and readjust on the graphene lattice during an AIMD run followed by DFT optimization. For graphene-supported K-Se cathode, optimized a-K₂Se/Gr configuration was considered the final discharged product (Figure 2c). Starting from this a-K₂Se/Gr structure, 6 K atoms were sequentially removed, followed by AIMDs and complete energy optimization, until a-Se₃₀/Gr is left (Figure 2d). Removal of K atoms at each step was completely random, and the system atoms were allowed to diffuse to find equilibria during the following AIMD run and optimization. Upon complete charging (depotassiation), the end structure resembles a-Se clusters distributed on a periodic graphene mesh (Figure 2d). This computationally modeled configuration is close to experimentally synthesized nano architectures of active electrodes and graphene. 39,41,45,46

2.2. Computational Details. All AIMD and DFT simulations were performed in Vienna Ab initio Simulation Package (VASP). Inert core electrons were mimicked by projector-augmented-wave (PAW) potentials and valence electrons were represented by plane-wave basis set with energy cut off at 550 eV. The GGA-PBE exchange-correlation function was taken into account for all calculations. AIMD simulations were run with 1 fs time interval, temperature set at 300 K within NVT ensemble, and $2 \times 2 \times 2$ gamma centered k-meshes. For all DFT calculations, the conjugate gradient

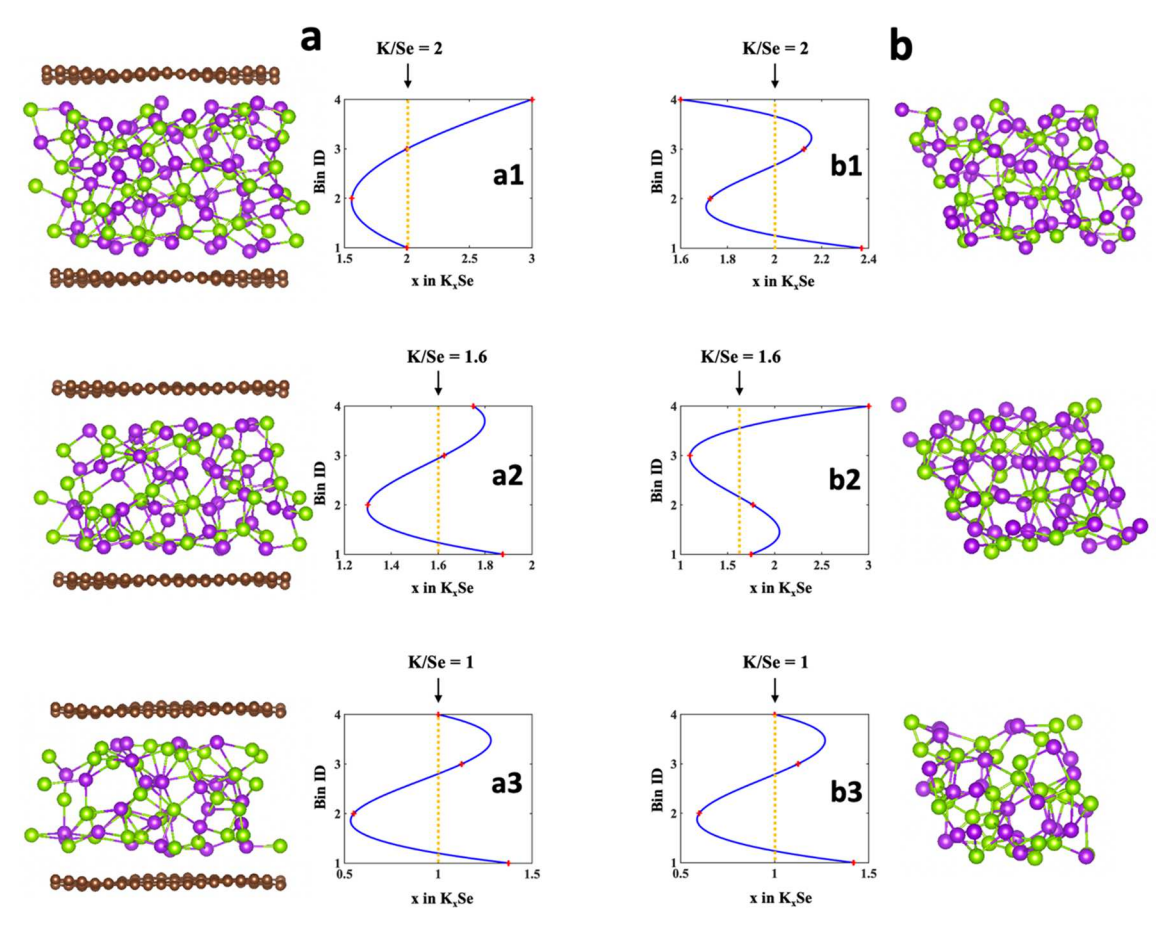


Figure 3. Degree of K segregation and K/Se ratio profile for (a) periodic a- K_x Se/Gr and (b) periodic a- K_x Se without any graphene support. Structures are divided into four bins along the z dimension noted as bin ID 1–4. K/Se ratios in each bin are marked with red and connected by a blue line to preview the pattern. Average K/Se ratio in the entire bulk is plotted as a dashed yellow line for comparison purpose. (a1) Marked K/Se ratios across the cathode thickness in completely discharged a- K_2 Se/Gr. (a2) Marked K/Se ratios across the cathode thickness in high K cathode a- K_1 6Se/Gr. (a3) Marked K/Se ratios across the cathode thickness in cathode a-KSe/Gr. (b1) Marked K/Se ratios across the cathode thickness in cathode a-KSe. (b2) Marked K/Se ratios across the cathode thickness in high K cathode a- K_1 6Se. (b3) Marked K/Se ratios across the cathode thickness in cathode a-KSe. Graphene supported cathodes with overall high average K ratio(>1) demonstrate higher K concentrations closer to graphene surface (bin ID 1 and 3). In periodic a- K_x Se cathodes without a graphene—substrate, the K concentration peaked alternatively in bins. In cathodes with lower average K/Se ratios (\leq 1), distribution of K is nearly the same irrespective of graphene presence.

method was employed for energy minimization with Hellmann–Feynman forces less than 0.02 eV/Å and convergence tolerance set to 1.0×10^{-4} eV. Gamma-centered $4\times4\times4$ k-meshes were taken for good accuracy. Only for graphene-supported cathodes, GGA functional was inclusive of vdW correction to incorporate the effect of weak long-range van der Waals (vdW) forces. All calculations for graphene-supported cathode were done with optPBE functional within vdW-DF-family. S2,53

3. RESULTS AND DISCUSSION

3.1. Potassium Segregation at the Interface. The presence of graphene—substrate is reportedly beneficial for the Se electrode to control the dissolution of polyselenides in electrolytes and provide a supportive matrix to the volume fluctuating electrode. However, graphene and pristine as Se do not form a very reliable interface from a physicochemical perspective. On a positive note, low interface strength (0.34 J/m²) between Se and graphene indicates Se electrode interfaced with graphene can easily expand/contract during the battery cycle and evade high mechanical stresses. On the downside, the two materials are held by weak van der Waals (vdW) forces and have a very high potential gradient at

the interface.³⁸ This condition is subjected to change as K atoms enter the Se bulk due to prospective phase changes and different binding affinities of both atom types with graphene. Therefore, we expect distinct microstructural order in graphene supported a-K_xSe cathode from its free counterpart. Figure 3 presents relaxed atomic structures of a-K_xSe cathodes with and without graphene—substrate, together with the respective variations of the atomic K/Se ratio along the *z*-dimension.

To determine the influence of the graphene—substrate on the distribution of K and Se atoms, the atomic K/Se ratio profile is traced in three high K cathode configurations: a- K_2 Se, a- $K_{1.6}$ Se, and a-KSe. Figure 3a demonstrates the K/Se ratio profiles in cathode configurations with a graphene support, while their graphene-free counterparts are analyzed in Figure 3b. Simulation cells are divided into four bins (bin ID = 1, 2, 3, 4) along the z-direction. In graphene-supported structures, the bottom 3.4 Å is not included in the bins considering it to be the vdW radius of graphene and represents the volume occupied by only graphene. The rest of the simulation cell (z-3.4 Å) is divided into bins of width ranging from 3.18 to 3.8 Å depending upon the a- K_x Se thickness. For graphene-free a- K_x Se, bin widths ranged between 3.6 and 4 Å. The atomic K/

Se ratios in each bin are marked with red and connected by blue line to view the pattern. The average K/Se ratio in the entire bulk (x in a-K $_x$ Se) is plotted as a dashed yellow line for comparison purposes.

In graphene-supported a-K_xSe (Figure 3a), two prominent regions can be noted based on K/Se ratio analysis: K-rich and K-deficient. K/Se ratios in bins 1 and 4 (close to the graphene surface) clearly demonstrate higher K concentration (Figure 3a). In contrast, bin 2 (further from the graphene surface) has a low K concentration in all three cathode configurations (Figure 3a), i.e., x in $K_xSe = 2$, 1.6, and 1. The combined K/Se ratio in bins 1 and 4 is continually above the average (yellow line) bulk K/Se ratio. A clear K concentration gradient is observed in the subinterfacial region (bin ID 1, 4) and central region (bin ID 2, 3). These plots indicate the affinity of the K atom to the graphene surface and the possibility of K segregation at the interface. The balance of K concentration in the electrode could be decided by observing bin-wise K/Se ratios (red) with respect to the average value (yellow line). The K concentration in completely discharged cathode a-K₂Se/Gr appears to be balanced. As shown in Figure 3a1, bins 1 and 3 have an average K/Se concentration value (i.e., x = 2) that falls on the yellow line. However, K/Se concentration values in bins 2 and 4 are less and more than the average (x =2), respectively. In contrast, for a-K_{1.6}Se/Gr and a-KSe/Gr shown in Figure 3a2,a3, K concentrations are higher than the average (x = 1.6 and x = 1, respectively) in three out of four bins (bins 1, 3, 4) suggesting a misbalance of K distribution in intermediate cathode structures.

The plots in Figure 3b represent K/Se ratios in graphenefree a-K_rSe cathode configurations and demonstrate alternative fluctuations of K/Se ratios within bins. It is important to remember that in these atomic representations of cathodes without graphene, a-K_rSe are continuous periodic bulks. Understandably, a bin with high K concentration is followed by a bin with low K concentration. No distinct pattern of K distribution can be recognized without a substrate. Moreover, the K/Se ratio plot for low K concentration(K/Se ≤ 1) cathode in Figure 3b3 is similar to that of the graphenesupported one in Figure 3a3, indicating that at low K content, segregation effect of graphene is reduced. Furthermore, all a-K_xSe structures in our study remained amorphous for both graphene-supported and graphene-free cases, as elaborated in the next section. It is unclear whether the segregation of K atoms at the graphene interface causes the formation of any new phase or phase boundary. The system size considered in our atomic study is too small to determine any phase transitions and phase boundaries. Nevertheless, the presence of graphene-substrate creates a significant chemical gradient inside K-Se cathode intermediates (Figure 3a) and an imbalance in K concentration. This affects the site-specific energy of K atoms in the cathode⁵⁴ and the stability of structural intermediates.

3.2. Microstructural Analysis. We observe in previous section that the presence of graphene causes a K concentration gradient in the active K_x Se cathode. Additionally, earlier reports³⁸ suggest that graphene interface can make the electronic states in a-Se more continuous and the system more conductive. In a reciprocal manner, the electronegative Se manipulates the surface chemistry of graphene—substrate and activates it to provide additional ion storage sites. ^{23,55,56} In this section, we provide evidence that despite having a

nonreactive surface, pristine graphene can enhance K-Se reactivity at the interface.

We first investigate the short-range and long-range structural configuration of the present systems by radial distribution function (RDF) analysis. The nearest neighboring distances between the atom pairs (Se–Se, Se–K, and K–K) in a- K_x Se cathodes from RDF analysis are represented in Figure 4.

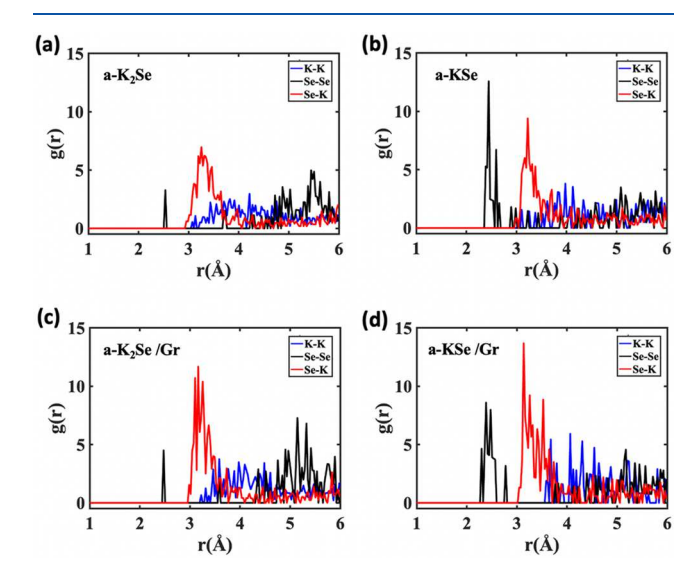


Figure 4. Radial distribution function (RDF) plots exhibiting nearest neighboring distances between atomic pairs in graphene free configurations (a) a- K_2 Se, (b) a- K_3 Se, and graphene-supported configurations (c) a- K_2 Se/Gr and (d) a- K_3 Ce/Gr. Distances between atomic pairs are plotted as Se–Se with black, Se–K with red, and K–K with blue.

Crystallinity is recognized by sharp singular distinct peaks in the plots, while broad peaks are characteristic of the amorphous structure. RDF plots of completely discharged and partly discharged a- K_x Se (x = 2 and 1) configurations in the graphene-supported systems (Figure 4c,d) are compared with graphene-free cases (Figure 4a,b). The important peaks for neighboring distances between Se–Se, Se–K, and K–K atomic pairs are listed in Table 1. Crystalline c- K_2 Se and c- K_3 Se

Table 1. Nearest Neighboring Distances (Å) between Se–Se, Se–K, and K–K in the K_xSe Cathodes with and without Graphene–Substrate^a

System	Se-Se	Se-K	K-K	Characteristic
a-K ₂ Se	2.5, 4.9, 5.5	3.25	>3	Amorphous
a-K ₂ Se/Gr	2.4, 4.4, 5.2	3.2	>3.2	Amorphous
c-K ₂ Se	5.5	3.35	3.8	Crystalline
a-KSe	2.5	3.2	>3.0	Amorphous
a-KSe/Gr	2.5, 2.8	3.2	>3.5	Amorphous
c-KSe	2.5, 3.7, 5.2	3.3, 3.5	4.3, 4.9, 5.4	Crystalline

"Note: "a-" denotes an amorphous structure and "c-" denotes crystalline structures.

systems are obtained from Materials Project database and their RDF analysis is used as a comparative standard to identify any sign of short-range crystalline order in amorphous atomic systems in our study.⁵⁷ In c-K₂Se (Figure S1a), the nearest neighboring distance of 5.5 Å for the Se–Se atom pair denotes that no Se–Se covalent bonds are present in the structure. Similarly, no K–K bond pairs are present in the same

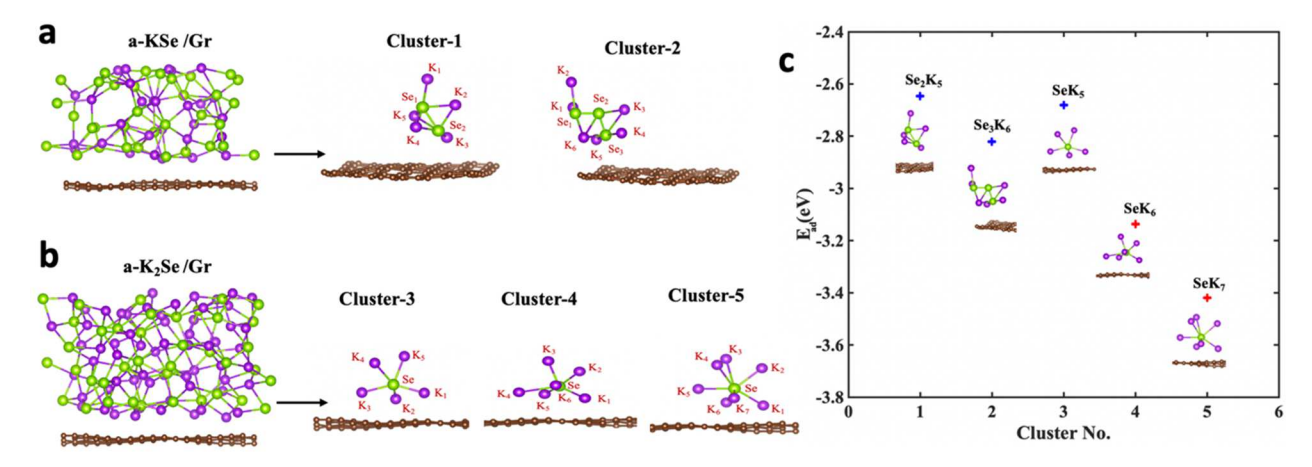


Figure 5. (a) Side view of the relaxed a-KSe/Gr structure. Majority Se—Se bonds are intact, and interface contains potassium polyselenides with two to three Se atom chains at the center. These clusters are numbered as 1 and 2. (b) Side view of the relaxed a- K_2 Se/Gr structure. Majority Se—Se bonds have broken to accommodate K and interface contains Se—K clusters with one Se atom at the center surrounded by K atoms. Clusters are numbered as 3, 4, and 5. (c) Binding energies E_{ad} of different K—Se clusters noted at the interface with the graphene—substrate. E_{ad} of clusters 4 and 5 which are least stable in the isolated state but bind strongly with graphene are marked in red.

structure. All Se atoms are bonded with K atoms with the bond length of 3.35 Å in the crystal configuration shown in Supporting Information SI-1. In contrast, we observe more Se—Se bond pairs with bond length of 2.5 Å in the atomic configuration of c-KSe with low K content (as shown in Figure S1b).

In graphene-free cathodes, the existence of long-range amorphous characteristics can be concluded from the RDF analysis. Black peaks at 2.5 Å in RDF plots indicate the presence of a few Se-Se covalent bonds. This peak is smaller and narrower in a high K concentration cathode (a-K₂Se), while it is intense and broader in a low K concentration cathode (a-KSe). Since the concentration of K is twice the Se in a-K₂Se, Se-K bonds are prominent observations in Figure 4a with bond lengths of ~ 3.25 and 3.35 Å. The red peaks at 2.9-3.4 Å are representative of Se-K distances and have a broad base. These peaks strongly contrast with very defined RDF plots of crystalline configurations in Figure S1. In both a-K_xSe systems, K forms strong covalent bonds with Se. Hence, no prominent K–K bond pairs are noticed in the RDF analysis. The K-K values in Table 1 represent the neighboring distances and not the bond lengths. RDF plots for graphenesupported cathodes in Figure 4c,d show intense red peaks that are representative of the Se-K bond. This increase in Se-K bond pairs along with evidence of K segregation at the interface in previous section presents a strong cue that graphene induces reactivity between Se and K in the system. Though it remains unclear if the presence of graphenesubstrate induces any short-range crystallinity in the cathodes or not, graphene undoubtedly enhances K reactivity at the interface.

One stand-alone difference between high K cathode (a- K_2Se) and low K cathode (a-KSe) configurations in Figure 4 is the peak intensity at 2.5 Å for Se–Se bonds. As mentioned earlier, a small peak at 2.5 Å in a- K_2Se (both graphene-free and graphene-supported cathodes) indicates the presence of only a few Se–Se covalent bonds. This peak becomes very prominent in a-KSe (both graphene-free and graphene-supported cathodes), signifying that Se–Se bonds are more profound. Se retains their chained structures at low K concentrations. This causes key differences in the Se–K microstructures that are observed in low-K (a-KSe/Gr) and high-K (a- K_2Se/Gr)

cathodes interfaced with graphene. In low K cathodes, the majority Se-Se bonds are intact, and the interface contains potassium polyselenides with two to three Se atoms at the center surrounded by K atoms. When the K concentration is further lowered (x < 1 in K_x Se), Se chains become longer. Meanwhile, as the K concentration increases, most Se-Se bonds break to accommodate K. The resulting interface contains Se-K clusters with one Se atom at the center bound by multiple K atoms. Inspired by these inferences, we analyzed the Se-K clusters at graphene interface in a-KSe/Gr and a- K_2Se/Gr to determine their adsorption energy E_{ad} over the graphene surface. Polyselenides in a-KSe/Gr (Figure 5a) are labeled as cluster-1 (Se-Se) and cluster-2 (Se-Se-Se). As discussed earlier, a-KSe/Gr has been created after sequential depotassiation from a-K₂Se/Gr. Hence, Se-Se bonds in a-KSe/Gr are formed after K was removed (charging) and are not present due to the initial a-Se₃₀ chain structure. Meanwhile, K saturation in a-K₂Se/Gr causes each Se atom to be surrounded by many K atoms (4 to 7). Typically, three Se-K clusters are present at the interface: Se₁K₅, labeled as cluster-3, Se₁K₆, labeled as cluster-4, and Se₁K₇, labeled as cluster-5 (Figure 5b). Only the Se atoms present near the graphene surface (bin ID 1) are bound to 6 or 7 K atoms, while Se in the central region (bin ID 2 and 3) are bound to 4 or 5 K atoms.

The surface adsorbed clusters were isolated from the bulk, and their adsorption energies (E_{ad}) over graphene—substrate were determined as follows

$$E_{ad} = E_{total} - E_{cluster} - E_{graphene} \tag{1}$$

where E_{total} is the energy of cluster over graphene—substrate determined by DFT, $E_{cluster}$ and $E_{graphene}$ are the energy of the isolated cluster and pristine graphene—substrate. Negative E_{ad} denotes thermodynamically favored adsorption. We do not consider distinct translational or rotational configurations of Se–K clusters and limit our analysis to their existing orientation found in the parent bulk models (a-KSe/Gr and a-K₂Se/Gr). Stability of isolated clusters is realized from $E_{cluster}$ values (Figure 5c) in the order cluster-2 > cluster-1 > cluster-3 > cluster-4 > cluster-5. Polyselenides (cluster-1 and -2) are naturally more stable than high-K clusters (cluster-4 and -5). Our thermodynamic values indicate that high-K clusters cannot exist independently outside the graphene-supported

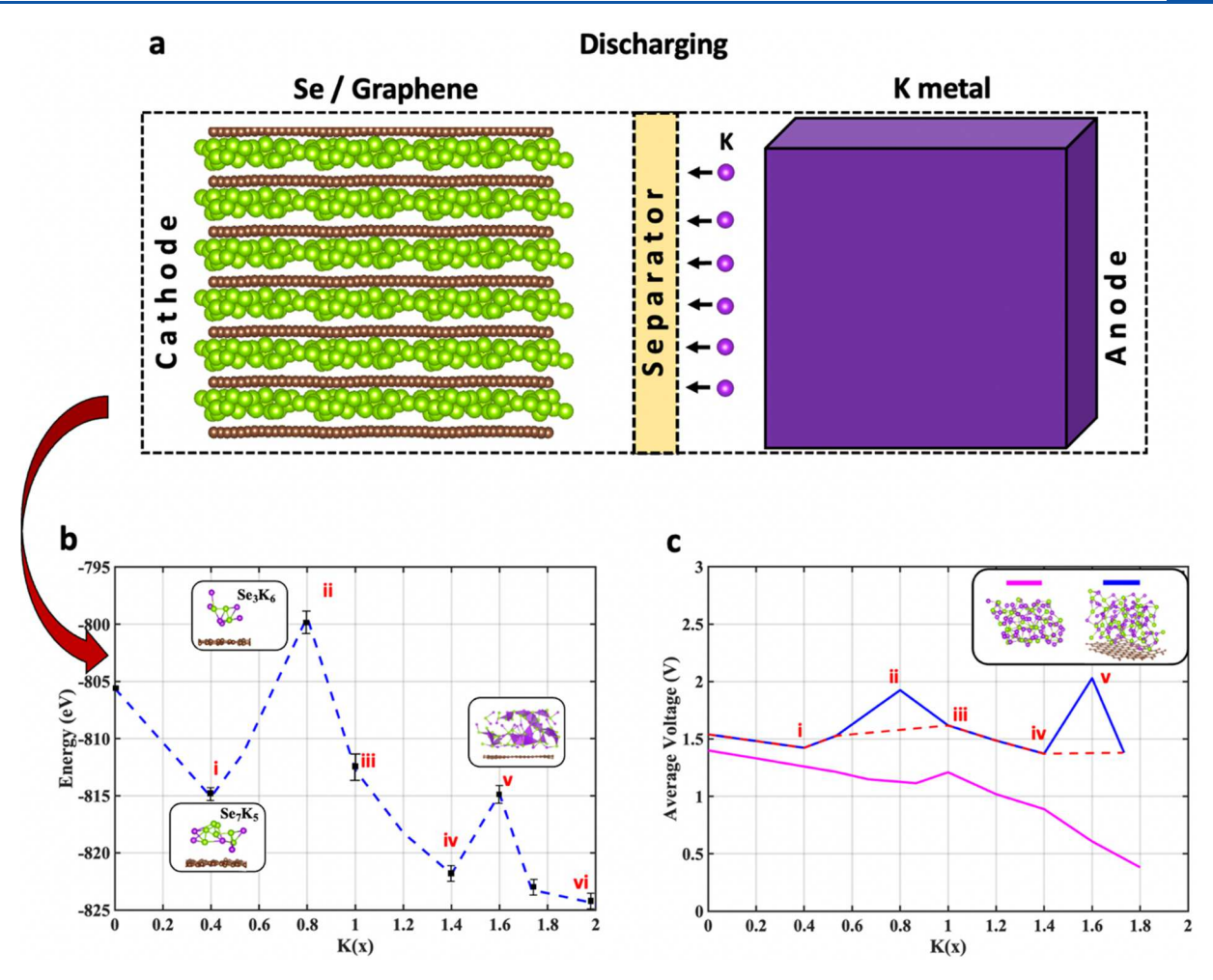


Figure 6. (a) Selenium-graphene heterostructure cathode half-cell during the discharging process in KIB. (b) Energy of relaxed graphene supported a- K_x Se ($0 \le x < 2$) cathode intermediates labeled i to vi. (c) Average discharge voltage of a- K_x Se cathode intermediates with K_2 Se as the final discharged product. The voltage profiles of Se–K alloying cathode with and without graphene—substrate are plotted in blue and pink, respectively.

cathode bulk. Therefore, high-K clusters prefer to strongly bind to the graphene surface with the highest binding energies marked in red in Figure 5c (-3.137 eV for cluster-4 and -3.419 eV for cluster-5). Interaction strength of the other three clusters (marked in blue in Figure 5c) with graphene is also reasonably high upon comparison with the literature. Thus, Se-K reaction intermediates are less likely to diffuse in the electrolyte to cause shuttle effects because of their strong binding affinity with graphene—substrate. Among interfacial clusters in the low K cathode, cluster-2 (Se-Se-Se centered) is more stable and interacts more strongly with the graphene—substrate. As we observed an increase in binding energy with increase in Se content (Se-Se to Se-Se-Se), discharging may not be very favorable over graphene surface in low K cathode intermediates (with increased Se_n chains). S8,59

Our previous study on physiochemical analysis of the Se-Gr interface shows that loose Se (Se_1) atoms of a-Se that are present in the interfacial region exhibit individualism and adsorb on graphene surface by gaining electrons leading to p-type doping in the latter. Once Se chains dissociate at high K concentrations, K starts to accumulate in the interfacial region because of their strong binding affinity with graphene. Presence of K in the interfacial region counteracts the doping characteristics of graphene. Density of states (DOS) analysis (see Supporting Information SI-2) exhibits a negative shift in

the Dirac cone of graphene in the presence of high K clusters, indicating n-type doping characteristics. In the presence of high K near the interface, graphene gains more electrons and presents an electron rich surface that acts as an electrocatalyst for further Se–K reactivity in the interfacial region. However, these effects could be highly regional on the graphene surface leading to irregular K distribution. This is because mobility of charge carriers has been previously shown to decrease with increase in K surface dopants.⁶¹

3.3. Electrochemical Mechanism. Operation of KIB is based on the rocking-chair principle of LIBs, with K ions shuttling between anode and cathode through an electrolyte. To navigate this K ion shuttling, a chemical potential difference must exist between cathode ($\mu^{cathode}$) and anode (μ^{anode}), which is referred to as open circuit voltage (OCV).

$$OCV = -\frac{\mu_K^{cathode} - \mu_K^{anode}}{zF}$$
 (2)

Here, F is Faraday's constant, and z is the electronic charge transported by K in the electrolyte (z = 1 for K in a nonconducting electrolyte). To theoretically calculate OCV for the K_x Se cathode, the K metal anode is considered with a constant chemical potential equivalent to the K metal's Gibbs free energy (depicted in Figure 6a). Thus, the electrical energy 62 gained in discharging between K_y Se and K_x Se (x > y)

is given by the difference in Gibbs free energy (G) of the two compounds as

$$E = -[G_{K_x Se} - G_{K_y Se} - (x - y)G_K]$$
(3)

$$E = -\Delta G \tag{4}$$

where G_K is the total Gibbs free energy of a single K atom in metallic K unit cell, and (x-y) represents K atoms intercalated in the cathode during discharging. This leads us to calculate the average intercalation voltage in cathode between two intercalation limits as

$$V = \frac{E}{(x - y)F} \tag{5}$$

Gibbs free energies calculated in our study are in electronvolts (eV) and are plotted for intermediate a-K_rSe/ Gr structures $(0 \le x < 2)$ in Figure 6b. Therefore F is neglected in the above equation. 63 Average voltage profiles between final discharged cathode a-K2Se and cathode intermediates (a- K_x Se with $0 \le x < 2$) as a function of K content are shown in Figure 6c. A sloping voltage curve in the range 1.4-0.38 V (pink curve in Figure 6c) is the result of amorphous Se forming a solid solution with K in the absence of any substrate. The voltage plot slopes downward with a small spike at x = 1 (KSe). It is suggestive of a two-step reaction process where K₂Se₂ (KSe) is initially formed before being further reduced to K₂Se, the final discharged product. We must mention here that different reported reduction pathways exist for Se in K–Se batteries based on electrolytes and Se microstructures. 64,65 Se_n chains undergo a single-step conversion to K2Se in carbonate-based electrolytes, which can sometimes become two-step conversion due to low reactivity $(Se \rightarrow K_2Se_2 \rightarrow K_2Se)$. Alternatively, several intermediate K_xSe are formed during Se_n reduction when ether-based electrolytes are used.⁶⁴ Since electrolytic influences are not taken into consideration in the present study, we can safely assume that electrochemical mechanisms observed here are purely driven by the Se molecular structure. As previously established, the Se cathode cannot successfully operate without any host matrix. The capacity of pristine Se in KIB has been previously shown to drop to zero after the first electrochemical cycle regardless of using carbonate-based electrolytes.²⁵ Thus, the high theoretical capacity of Se cathode can only be leveraged by combining Se with a C-based matrix.⁶

In comparison to porous C, the hexagonal C lattice-based matrix enclosing Se cathodes exhibit better performances for LIB. 41,46,66,67 $\check{\text{Th}}$ is partly due to high conductivity of hexagonal C lattice and partly due to inability of Se to form covalent interactions with lattice surface, thereby preventing the loss of active Se electrode. 38 Moreover, the host matrix can also have a significant impact on electrochemical reactions in the Se cathode. This concept is less understood in the literature mostly due to complex design of Se-based composite cathodes. The blue plot in Figure 6c shows the intercalation voltage profile of a-KxSe cathode supported by a hexagonal C lattice, i.e., graphene in this case. Major inferences that can be drawn from the plot are: first, the discharge voltage for intercalation limit x = 0 and x = 2 is 1.55 V, and second, multiple reaction products may be present in the system due to the incomplete reaction of Se.

Two high voltage peaks are noted at x = 0.8 and x = 1.6 in the blue plot of Figure 6c. These peaks correspond to the high-energy structures ii and v, as indicated in Figure 6b. The energy

of a-Se/Gr cathode dips during the discharging process, except near intermediates ii and v where the sudden energy spikes are noted. The plot indicates a difficult electrochemical reduction of Se cathode with possible formation of multiple reaction products. From an atomistic point of view, the rise in energy between intermediates *i* and *ii* is due to the stability of long Se chains on the graphene surface (Se-Se-Se vs Se-Se in Figure 6c) that causes an inconvenience in discharging. The higher binding affinity between graphene and polyselenides with increased Se content (Se-Se to Se-Se-Se) could cause difficulty in Se chain breakage to store more K. Post this stage (x = 0.8), Se continues to react with incoming K until high K concentration (x = 1.6) is reached corresponding to peak v. We know from our discussion in Sections 3.1 and 3.2 that graphene is causing strong K segregation at the interface in high K intermediates and impacting the electrochemical reaction by inducing new reactive sites near the interface. This causes irregular distribution of K through the cathode resulting in incomplete Se reduction at x = 1.6 (K₁₆Se). Similar peaks (like in Figure 6b) are reported in previous studies where electrode was recognized to constitute two distinct phases. 68,69 While the detailed microstructural and electrochemical analysis of graphene supported Se-K cathode strongly suggest possibility of multiple phases in the system, it is challenging to draw conclusions from nanoscale system. Possibility of interface-induced phase changes in these heterostructure electrodes could be further explored by multiscale modeling. Upon further discharging (K intercalation), all Se present in the system reacts with K to form a thermodynamically stable discharged product K₂Se. We deduce that graphene has modulating favorability toward discharging of Se cathode due to its surface characteristics and differential preferences for K_xSe intermediate systems.

From Figure 6c, we draw that operating a-Se/Gr cathode at high voltage conditions (\sim 2 V) can lead to the formation of cathode intermediates (ii and v) which represent thermodynamical energy barriers in the process of intercalation/deintercalation and could cause irreversible capacity losses. If we observe the intercalation voltage profile in Figure 6c upon ignoring these thermodynamical barriers (dashed red plot), the voltage remains in the 1.55–1.38 V range and exhibits a plateau-like profile. It is possible for Se to undergo a single-step reaction with K to form K_2 Se if the applied voltage is 1.55 V, much like in the case of Li–Se.

$$Se + 2K^{+} + 2e^{-} \rightarrow K_{2}Se$$
 (6)

This voltage range for electrochemical reaction is also close to cathode voltage reported in a study with Se hosted by carbon nanotube anchored microporous C.²⁷ Our results feature a strong dependence of Se–K electrochemistry on the interface presented by the graphene matrix in nanostructured electrodes.

4. CONCLUSIONS

To conclude, we modeled the graphene-supported K_x Se cathode identical with experimentally designed electrodes and investigated the effect of the graphene interface on the electrochemical mechanism by AIMD and DFT. Our results are the first to highlight strong dependence of the electrochemical mechanism in the Se cathode on the host structure. The key findings presented in the study are as follows:

- Graphene—substrate causes a substantial chemical gradient inside the K—Se cathode by inducing enhanced Se—K reactivity in the interfacial region.
- Surface chemistry of graphene interfaced with K_xSe cathode modulates based on its differential preference for Se and K atoms. At low K concentrations, graphene causes difficult K intercalation (discharging) because of its strong binding preference with longer Se_n chains (E_{ad} = −2.646 eV for n = 2 and E_{ad} = −2.82 eV for n = 3). Meanwhile at high K concentrations, K density near interface increases, causing the formation of Se−K clusters with a high K atom count (SeK₆, SeK₇). These clusters are not stable without substrate and interact strongly with graphene surface through binding energies (E_{ad}) as high as −3.137 eV for SeK₆ and −3.419 eV for SeK₇.
- This modulating favorability of graphene toward discharging of Se cathode could cause formation of reaction intermediate with thermodynamically challenging K insertion and extraction.
- To avoid irreversible capacity losses, graphene-supported Se cathode should operate in the voltage range of 1.55 to 1.38 V, which will lead to a single step reaction near 1.55 V with K₂Se as discharged product.

ASSOCIATED CONTENT

Data Availability Statement

The data reported in this paper is available from the corresponding author upon reasonable request.

Solution Supporting Information

The Supporting Information is available free of charge at https://pubs.acs.org/doi/10.1021/acsaem.3c00989.

Radial distribution function (RDF) of crystalline K_x Se and density of states (DOS) analysis of high K clusters with graphene surface (PDF)

Accession Codes

The pre- and postprocessing codes used in this paper are available from the corresponding author upon reasonable request. Restrictions apply to the availability of the simulation codes, which were used under license for this study.

AUTHOR INFORMATION

Corresponding Author

Vidushi Sharma — Department of Mechanical and Industrial Engineering, New Jersey Institute of Technology, Newark, New Jersey 07103, United States; orcid.org/0000-0002-4576-4990; Email: vs574@njit.edu, vidushis@ibm.com

Author

Dibakar Datta — Department of Mechanical and Industrial Engineering, New Jersey Institute of Technology, Newark, New Jersey 07103, United States; orcid.org/0000-0003-0233-3581

Complete contact information is available at: https://pubs.acs.org/10.1021/acsaem.3c00989

Author Contributions

V.S. contributed to the work with conception of the project, computation, and manuscript preparation. D.D. discussed results with V.S. and contributed to the manuscript

preparation. All authors have given approval to the final version of the manuscript.

Notes

The authors declare no competing financial interest.

ACKNOWLEDGMENTS

V.S. and D.D. were supported by NSF (Award Numbers 1911900 and 2237990) during the study. D.D. acknowledges the Extreme Science and Engineering Discovery Environment (XSEDE) for the computational facilities (Award Number DMR180013).

REFERENCES

- (1) Dahn, J. R.; Zheng, T.; Liu, Y.; Xue, J. Mechanisms For Lithium Insertion in Carbonaceous Materials. *Science* **1995**, *270* (5236), 590–593.
- (2) Whittingham, M. S. Electrical Energy Storage and Intercalation Chemistry. *Science* **1976**, *192* (4244), 1126–1127.
- (3) Zhang, W.; Liu, Y.; Guo, Z. Approaching High-Performance Potassium-Ion Batteries via Advanced Design Strategies and Engineering. Sci. Adv. 2019, 5 (5), No. aav7412.
- (4) De La Llave, E.; Borgel, V.; Park, K.-J.; Hwang, J.-Y.; Sun, Y.-K.; Hartmann, P.; Chesneau, F.-F.; Aurbach, D. Comparison Between Na-Ion and Li-Ion Cells: Understanding The Critical Role of the Cathodes Stability and the Anodes Pretreatment on the Cells Behavior. ACS Appl. Mater. Interfaces 2016, 8 (3), 1867–1875.
- (5) Palomares, V.; Serras, P.; Villaluenga, I.; Hueso, K. B.; Carretero-González, J.; Rojo, T. Na-Ion Batteries, Recent Advances and Present Challenges to Become Low Cost Energy Storage Systems. *Energy Environ. Sci.* **2012**, *5* (3), 5884–5901.
- (6) Eftekhari, A. Potassium Secondary Cell Based on Prussian Blue Cathode. *J. Power Sources* **2004**, *126* (1–2), 221–228.
- (7) Komaba, S.; Itabashi, T.; Kimura, T.; Groult, H.; Kumagai, N. Opposite Influences of K+ Versus Na+ Ions as Electrolyte Additives on Graphite Electrode Performance. *J. Power Sources* **2005**, *146* (1–2), 166–170.
- (8) Pramudita, J. C.; Sehrawat, D.; Goonetilleke, D.; Sharma, N. An Initial Review of the Status of Electrode Materials for Potassium-Ion Batteries. *Adv. Energy Mater.* **2017**, *7* (24), 1602911.
- (9) Komaba, S.; Hasegawa, T.; Dahbi, M.; Kubota, K. Potassium Intercalation into Graphite to Realize High-Voltage/High-Power Potassium-Ion Batteries and Potassium-Ion Capacitors. *Electrochem. commun.* **2015**, *60*, 172–175.
- (10) Nobuhara, K.; Nakayama, H.; Nose, M.; Nakanishi, S.; Iba, H. First-Principles Study of Alkali Metal-Graphite Intercalation Compounds. *J. Power Sources* **2013**, 243, 585–587.
- (11) Han, M. H.; Gonzalo, E.; Singh, G.; Rojo, T. A Comprehensive Review of Sodium Layered Oxides: Powerful Cathodes for Na-Ion Batteries. *Energy Environ. Sci.* **2015**, 8 (1), 81–102.
- (12) Vaalma, C.; Giffin, G. A.; Buchholz, D.; Passerini, S. Non-Aqueous K-Ion Battery Based on Layered K0. 3mno2 and Hard Carbon/Carbon Black. *J. Electrochem. Soc.* **2016**, *163* (7), A1295.
- (13) Zhang, C.; Xu, Y.; Zhou, M.; Liang, L.; Dong, H.; Wu, M.; Yang, Y.; Lei, Y. Potassium Prussian Blue Nanoparticles: A Low-Cost Cathode Material for Potassium-Ion Batteries. *Adv. Funct. Mater.* **2017**, 27 (4), 1604307.
- (14) Nossol, E.; Souza, V. H.; Zarbin, A. J. Carbon Nanotube/ Prussian Blue Thin Films as Cathodes for Flexible, Transparent and ITO-Free Potassium Secondary Battery. *J. Colloid Interface Sci.* **2016**, 478, 107–116.
- (15) Wessells, C. D.; Peddada, S. V.; Huggins, R. A.; Cui, Y. Nickel Hexacyanoferrate Nanoparticle Electrodes for Aqueous Sodium and Potassium Ion Batteries. *Nano Lett.* **2011**, *11* (12), 5421–5425.
- (16) Su, D.; Mcdonagh, A.; Qiao, S. Z.; Wang, G. High-Capacity Aqueous Potassium-Ion Batteries for Large-Scale Energy Storage. *Adv. Mater.* **2017**, *29* (1), 1604007.

ı

- (17) Pang, Q.; Liang, X.; Kwok, C. Y.; Nazar, L. F. Advances in Lithium-Sulfur Batteries Based on Multifunctional Cathodes and Electrolytes. *Nat. Energy* **2016**, *1* (9), 1–11.
- (18) Xu, G.; Ding, B.; Pan, J.; Nie, P.; Shen, L.; Zhang, X. High Performance Lithium-Sulfur Batteries: Advances and Challenges. *J. Mater. Chem. A* **2014**, *2* (32), 12662–12676.
- (19) Su, D.; Zhou, D.; Wang, C.; Wang, G. Lithium-Sulfur Batteries: Toward High Performance Lithium-Sulfur Batteries Based on Li2S Cathodes and Beyond: Status, Challenges, and Perspectives. *Adv. Funct. Mater.* **2018**, 28 (38), 1870273.
- (20) Liu, L.; Hou, Y.; Wu, X.; Xiao, S.; Chang, Z.; Yang, Y.; Wu, Y. Nanoporous Selenium as a Cathode Material for Rechargeable Lithium-Selenium Batteries. *Chem. Comm* **2013**, 49 (98), 11515–11517
- (21) Lee, J. T.; Kim, H.; Oschatz, M.; Lee, D. C.; Wu, F.; Lin, H. T.; Zdyrko, B.; Cho, W. I.; Kaskel, S.; Yushin, G. Micro-and Mesoporous Carbide-Derived Carbon-Selenium Cathodes for High-Performance Lithium Selenium Batteries. *Adv. Energy Mater.* **2015**, *5* (1), 1400981.
- (22) Cui, Y.; Abouimrane, A.; Lu, J.; Bolin, T.; Ren, Y.; Weng, W.; Sun, C.; Maroni, V. A.; Heald, S. M.; Amine, K. (De) Lithiation Mechanism of Li/Ses X (X= 0–7) Batteries Determined by In Situ Synchrotron X-Ray Diffraction and X-Ray Absorption Spectroscopy. *J. Am. Chem. Soc.* **2013**, *135* (21), 8047–8056.
- (23) Yang, C. P.; Xin, S.; Yin, Y. X.; Ye, H.; Zhang, J.; Guo, Y. G. An Advanced Selenium-Carbon Cathode for Rechargeable Lithium-Selenium Batteries. *Angew. Chem., Int. Ed.* **2013**, *52* (32), 8363–8367.
- (24) Liu, H.; Wang, Q.; Sun, X.; Gou, H.; Zhang, C.; Wang, G. Carbon Host Pore Structure Regulation Boosting Fast and Stable Se-K Electrochemistry Towards Se-K Ion Capacitors. *Carbon* **2023**, 203, 141–151.
- (25) Liu, Y.; Tai, Z.; Zhang, Q.; Wang, H.; Pang, W. K.; Liu, H. K.; Konstantinov, K.; Guo, Z. A New Energy Storage System: Rechargeable Potassium-Selenium Battery. *Nano Energy* **2017**, *35*, 36–43.
- (26) Yang, T.; Niu, Y.; Liu, Q.; Xu, M. Cathode Host Engineering for Non-Lithium (Na, K And Mg) Sulfur/Selenium Batteries: A State-Of-The-Art Review. *Nano Mater. Sci.* **2023**, *5*, 119–140.
- (27) Zhou, X.; Wang, L.; Yao, Y.; Jiang, Y.; Xu, R.; Wang, H.; Wu, X.; Yu, Y. Integrating Conductivity, Captivity, and Immobility Ability into N/O Dual-Doped Porous Carbon Nanocage Anchored with CNT as an Effective Se Host for Advanced K-Se Battery. *Adv. Funct. Mater.* **2020**, *30* (43), 2003871.
- (28) Huang, X.; Wang, W.; Deng, J.; Gao, W.; Liu, D.; Ma, Q.; Xu, M. A Se-Hollow Porous Carbon Composite for High-Performance Rechargeable K-Se Batteries. *Inorg. Chem. Front.* **2019**, *6* (8), 2118–2125.
- (29) Huang, X.; Deng, J.; Qi, Y.; Liu, D.; Wu, Y.; Gao, W.; Zhong, W.; Zhang, F.; Bao, S.; Xu, M. A Highly-Effective Nitrogen-Doped Porous Carbon Sponge Electrode for Advanced K-Se Batteries. *Inorg. Chem. Front.* **2020**, *7* (5), 1182–1189.
- (30) Kim, J. K.; Kang, Y. C. Encapsulation of Se into Hierarchically Porous Carbon Microspheres with Optimized Pore Structure for Advanced Na-Se And K-Se Batteries. *ACS Nano* **2020**, *14* (10), 13203–13216.
- (31) Li, D.; Wang, L.; Cheng, X.; Yao, Y.; Jiang, Y.; Shi, P.; Wu, Y.; Wu, X.; Ma, C.; Yu, Y. Manipulating Selenium Molecular Configuration in N/O Dual-Doped Porous Carbon for High Performance Potassium-Ion Storage. *J. Energy Chem.* **2021**, *62*, 581–589.
- (32) Xu, R.; Yao, Y.; Wang, H.; Yuan, Y.; Wang, J.; Yang, H.; Jiang, Y.; Shi, P.; Wu, X.; Peng, Z.; et al. Unraveling the Nature of Excellent Potassium Storage in Small-Molecule Se@ Peapod-Like N-Doped Carbon Nanofibers. *Adv. Mater.* **2020**, 32 (52), 2003879.
- (33) Abouimrane, A.; Dambournet, D.; Chapman, K. W.; Chupas, P. J.; Weng, W.; Amine, K. A New Class of Lithium and Sodium Rechargeable Batteries Based on Selenium and Selenium-Sulfur as a Positive Electrode. *J. Am. Chem. Soc.* **2012**, *134* (10), 4505–4508.
- (34) Yang, C. P.; Xin, S.; Yin, Y. X.; Ye, H.; Zhang, J.; Guo, Y. G. An Advanced Selenium-Carbon Cathode for Rechargeable Lithium-

- Selenium Batteries. Angew. Chem., Int. Ed. 2013, 125 (32), 8521–8525.
- (35) Xue, P.; Zhai, Y.; Wang, N.; Zhang, Y.; Lu, Z.; Liu, Y.; Bai, Z.; Han, B.; Zou, G.; Dou, S. Selenium@ Hollow Mesoporous Carbon Composites for High-Rate and Long-Cycling Lithium/Sodium-Ion Batteries. *Chem. Eng. J.* **2020**, 392, 123676.
- (36) Ding, J.; Zhou, H.; Zhang, H.; Tong, L.; Mitlin, D. Selenium Impregnated Monolithic Carbons as Free-Standing Cathodes for High Volumetric Energy Lithium and Sodium Metal Batteries. *Adv. Energy Mater.* **2018**, 8 (8), 1701918.
- (37) Basu, S.; Suresh, S.; Ghatak, K.; Bartolucci, S. F.; Gupta, T.; Hundekar, P.; Kumar, R.; Lu, T.-M.; Datta, D.; Shi, Y.; et al. Utilizing Van Der Waals Slippery Interfaces to Enhance the Electrochemical Stability of Silicon Film Anodes in Lithium-Ion Batteries. *ACS Appl. Mater. Interfaces* **2018**, *10* (16), 13442–13451.
- (38) Sharma, V.; Mitlin, D.; Datta, D. Understanding the Strength of the Selenium-Graphene Interfaces for Energy Storage Systems. *Langmuir* **2021**, *37* (6), 2029–2039.
- (39) Han, K.; Liu, Z.; Ye, H.; Dai, F. Flexible Self-Standing Graphene-Se@ CNT Composite Film as a Binder-Free Cathode for Rechargeable Li-Se Batteries. *J. Power Sources* **2014**, 263, 85–89.
- (40) Huang, D.; Li, S.; Luo, Y.; Xiao, X.; Gao, L.; Wang, M.; Shen, Y. Graphene Oxide-Protected Three Dimensional Se as a Binder-Free Cathode for Li-Se Battery. *Electrochim. Acta* **2016**, *190*, 258–263.
- (41) Sha, L.; Gao, P.; Ren, X.; Chi, Q.; Chen, Y.; Yang, P. A Self-Repairing Cathode Material for Lithium-Selenium Batteries: Se- C Chemically Bonded Selenium-Graphene Composite. *Chem. Eur. J.* **2018**, *24* (9), 2151–2156.
- (42) Luo, C.; Xu, Y.; Zhu, Y.; Liu, Y.; Zheng, S.; Liu, Y.; Langrock, A.; Wang, C. Selenium@ Mesoporous Carbon Composite with Superior Lithium and Sodium Storage Capacity. *ACS Nano* **2013**, 7 (9), 8003–8010.
- (43) Escoffery, C.; Halperin, S. Studies on the Polymorphic Transformation of Selenium. *Trans. Electrochem. Soc.* **1946**, 90 (1), 163.
- (44) Goldan, A.; Li, C.; Pennycook, S.; Schneider, J.; Blom, A.; Zhao, W. Molecular Structure of Vapor-Deposited Amorphous Selenium. *J. Appl. Phys.* **2016**, *120* (13), 135101.
- (45) Peng, X.; Wang, L.; Zhang, X.; Gao, B.; Fu, J.; Xiao, S.; Huo, K.; Chu, P. K. Reduced Graphene Oxide Encapsulated Selenium Nanoparticles for High-Power Lithium-Selenium Battery Cathode. *J. Power Sources* **2015**, 288, 214–220.
- (46) Han, K.; Liu, Z.; Shen, J.; Lin, Y.; Dai, F.; Ye, H. A Free-Standing and Ultralong-Life Lithium-Selenium Battery Cathode Enabled by 3D Mesoporous Carbon/Graphene Hierarchical Architecture. *Adv. Funct. Mater.* **2015**, 25 (3), 455–463.
- (47) Kresse, G.; Furthmüller, J. Efficient Iterative Schemes for Ab Initio Total-Energy Calculations Using a Plane-Wave Basis Set. *Phys. Rev. B* **1996**, *54* (16), 11169.
- (48) Kresse, G.; Joubert, D. From Ultrasoft Pseudopotentials to the Projector Augmented-Wave Method. *Phys. Rev. B* **1999**, *59* (3), 1758.
- (49) Blöchl, P. E. Projector Augmented-Wave Method. *Phys. Rev. B* **1994**, *50* (24), 17953.
- (50) Perdew, J. P.; Burke, K.; Ernzerhof, M. Generalized Gradient Approximation Made Simple. *Phys. Rev. Lett.* **1996**, 77 (18), 3865.
- (51) Dion, M.; Rydberg, H.; Schröder, E.; Langreth, D. C.; Lundqvist, B. I. Van Der Waals Density Functional for General Geometries. *Phys. Rev. Lett.* **2004**, 92 (24), 246401.
- (52) Klimeš, J.; Bowler, D. R.; Michaelides, A. Chemical Accuracy for the Van Der Waals Density Functional. *J. Phys.: Condens. Matter* **2010**, 22 (2), 022201.
- (53) Klimeš, J.; Bowler, D. R.; Michaelides, A. Van Der Waals Density Functionals Applied to Solids. *Phys. Rev. B* **2011**, 83 (19), 195131.
- (54) Liu, C.; Neale, Z. G.; Cao, G. Understanding Electrochemical Potentials of Cathode Materials in Rechargeable Batteries. *Mater. Today* **2016**, *19* (2), 109–123.
- (55) Xue, P.; Zhai, Y.; Wang, N.; Zhang, Y.; Lu, Z.; Liu, Y.; Bai, Z.; Han, B.; Zou, G.; Dou, S. Selenium@ Hollow Mesoporous Carbon

- Composites for High-Rate and Long-Cycling Lithium/Sodium-Ion Batteries. Chem. Eng. J. 2020, 392, 123676.
- (56) Zhou, J.; Chen, M.; Wang, T.; Li, S.; Zhang, Q.; Zhang, M.; Xu, H.; Liu, J.; Liang, J.; Zhu, J.; et al. Covalent Selenium Embedded in Hierarchical Carbon Nanofibers for Ultra-High Areal Capacity Li-Se Batteries. *iScience* **2020**, 23 (3), 100919.
- (57) Jain, A.; Ong, S. P.; Hautier, G.; Chen, W.; Richards, W. D.; Dacek, S.; Cholia, S.; Gunter, D.; Skinner, D.; Ceder, G.; Persson, K. A. Commentary: The Materials Project: A materials genome approach to accelerating materials innovation. *APL Mater.* **2013**, *1* (1), No. 011002.
- (58) Xu, G.-L.; Liu, J.; Amine, R.; Chen, Z.; Amine, K. Selenium and Selenium-Sulfur Chemistry for Rechargeable Lithium Batteries: Interplay of Cathode Structures, Electrolytes, and Interfaces. *ACS Energy Lett.* **2017**, 2 (3), 605–614.
- (59) Mukherjee, S.; Kavalsky, L.; Chattopadhyay, K.; Singh, C. V. Adsorption and Diffusion of Lithium Polysulfides over Blue Phosphorene for Li-S Batteries. *Nanoscale* **2018**, *10* (45), 21335–21352.
- (60) Nakada, K.; Ishii, A. First-Principles Investigation of Charge Density Analysis of Various Adatom Adsorptions on Graphene. *AIP Conf Proc.* **2011**, 1399, 793–794.
- (61) Liu, H.; Liu, Y.; Zhu, D. Chemical Doping of Graphene. J. Mater. Chem. 2011, 21 (10), 3335–3345.
- (62) Aydinol, M.; Kohan, A.; Ceder, G.; Cho, K.; Joannopoulos, J. Ab Initio Study of Lithium Intercalation in Metal Oxides and Metal Dichalcogenides. *Phys. Rev. B* **1997**, *56* (3), 1354.
- (63) Ghatak, K.; Basu, S.; Das, T.; Sharma, V.; Kumar, H.; Datta, D. Effect of Cobalt Content on the Electrochemical Properties and Structural Stability of NCA Type Cathode Materials. *Phys. Chem. Chem. Phys.* **2018**, 20 (35), 22805–22817.
- (64) Huang, X. L.; Guo, Z.; Dou, S. X.; Wang, Z. M. Rechargeable Potassium-Selenium Batteries. *Adv. Funct. Mater.* **2021**, *31*, 2102326.
- (65) Eftekhari, A. The Rise of Lithium-Selenium Batteries. *Sustain. Energy Fuels* **2017**, *1* (1), 14–29.
- (66) Zhang, J.; Xu, Y.; Fan, L.; Zhu, Y.; Liang, J.; Qian, Y. Graphene-Encapsulated Selenium/Polyaniline Core-Shell Nanowires with Enhanced Electrochemical Performance for Li-Se Batteries. *Nano Energy* **2015**, *13*, 592–600.
- (67) Wang, X.; Zhang, Z.; Qu, Y.; Wang, G.; Lai, Y.; Li, J. Solution-Based Synthesis of Multi-Walled Carbon Nanotube/Selenium Composites for High Performance Lithium-Selenium Battery. *J. Power Sources* **2015**, 287, 247–252.
- (68) Wagemaker, M.; Mulder, F. M.; Van Der Ven, A. The Role of Surface and Interface Energy on Phase Stability of Nanosized Insertion Compounds. *Adv. Mater.* **2009**, *21* (25–26), 2703–2709.
- (69) Van Der Ven, A.; Garikipati, K.; Kim, S.; Wagemaker, M. The Role of Coherency Strains on Phase Stability in Li X Fepo4: Needle Crystallites Minimize Coherency Strain and Overpotential. *J. Electrochem. Soc.* **2009**, *156* (11), A949.
- (70) Li, Q.; Liu, H.; Yao, Z.; Cheng, J.; Li, T.; Li, Y.; Wolverton, C.; Wu, J.; Dravid, V. P. Electrochemistry of Selenium with Sodium and Lithium: Kinetics and Reaction Mechanism. *ACS Nano* **2016**, *10* (9), 8788–8795.